Double Paddle-Wheel Enhanced Sodium Ion Conduction in an

Antiperovskite Solid Electrolyte

Ping-Chun Tsai, Sunil Mair, Jeffrey Smith, David M. Halat, Po-Hsiu Chien, Kwangnam Kim, Duhan Zhang, Yiliang Li, Liang Yin, Jue Liu, Saul H. Lapidus, Jeffrey A. Reimer, Nitash P. Balsara, Donald J. Siegel,   Yet-Ming Chiang*

Ping-Chun Tsai

National Taiwan University of Science and Technology

Taipei City, Taiwan

S. Mair, D. Zhang, Y. Li, Y. Chiang

Massachusetts Institute of Technology

Cambridge, MA 02139, USA

Email Address: ychiang@mit.edu

J. Smith, K. Kim

University of Michigan, Ann Arbor

Ann Arbor, MI 48103, USA

D. Halat, J. A. Reimer, N. P. Balsara

University of California, Berkeley

Berkeley, CA 94720, USA

P. Chien, J. Liu

Oakridge National Laboratory

Oak Ridge, TN, 37830

L. Yin, S. H. Lapidus

Argonne National Laboratory

Lemont, IL 60439, USA

D. J. Siegel

University of

Texas at Austin

Austin, TX 78712,

USA

Antiperovskite structure compounds (X_3AB, where X is an alkali cation and A and B are anions) have the potential for highly correlated motion between the cation and a cluster anion on the A or B site. This so-called "paddle-wheel" mechanism may be the basis for enhanced cation mobility in solid electrolytes. Here we show, through combined experiments and modeling, the first instance of a double paddle-wheel mechanism, leading to fast sodium ion conduction in the antiperovskite $Na_{3-x}O_{1-x}(NH_2)_x(BH_4)$. As the concentration of amide (NH_2^-) cluster anions is increased, large positive deviations in ionic conductivity above that predicted from a vacancy diffusion model are observed. Using EIS, PXRD, synchrotron XRD, neutron diffraction, AIMD, and NMR, we characterize the cluster anion rotational dynamics, and find that cation mobility is influenced by the rotation of both NH_2^- and BH_4^- species, resulting in sodium ion conductivity a factor of 10^2 higher at $x = 1$ than expected for the vacancy mechanism alone. Generalization of this phenomenon to other compounds could accelerate fast ion conductor exploration and design.

Introduction

The performance of many electrochemical systems including batteries [1], hydrogen and solid oxide fuel cells [2, 3], and electrolytic reactors for production of raw materials such as aluminum and chlorine [4, 5] depends on the transport of specific working ions through an electrolyte. The nature of the electrolytes to be used in the electrochemical systems that will enable the burgeoning clean energy transition remains an important open question. While most contemporary battery electrolytes are liquids, which contain the working ion as a dissolved salt, solid-state electrolytes have the potential to bring about advances in terms of performance and safety [6, 7], as well as to enable electrochemical systems with novel architectures [8, 9]. For many decades, efforts aimed at achieving ionic conductivities in solids that rivaled or surpassed those of liquid electrolytes (on the order of 10 mS/cm) [10] yielded little progress, until the breakthrough discovery of $Li_{10}GeP_2S_{12}$ in 2011 [11]. The subsequent discovery of a number of ion-conducting solids with conductivities on par with those of liquids has generated intense interest in the development of all-solid-state batteries. A comprehensive understanding of ion transport mechanisms is critical to the design of solid-state fast ion conductors. Thus far, studies focused on the relationship between static structure and cation mobility have yielded significant improvements in ionic conductivity by understanding and leveraging features such as cation vacancy concentration [12], volume effects [13, 14], and concerted migration mechanisms [12, 15], amongst others [16, 17, 18, 19, 20]. Anion dynamics, specifically the rotation of cluster anions, may have an equally large effect on cation mobility but have yet to be understood to the same degree [21].

It has been observed that structures containing cluster anions (anions composed of multiple atoms bound by covalent bonds such as sulfate (SO_4^{2-}), nitrate (NO_2^-), phosphate (PO_4^{3-}) anions, etc., also known as "molecular anions," "polyanions," "complex anions," or "rotor groups") may show increased cation conductivity relative to analogous structures with single atom, spherically symmetric anions [22, 23, 24, 25, 26, 27]. This is known as the "paddle-wheel" effect, whereby correlated rotations of cluster anions allow for cation translation with lower migration energy barriers, resulting in higher cation mobility. Due to the relevant spatial and temporal scales (angstroms and picoseconds respectively), it has been challenging to physically characterize instances of the paddle-wheel mechanism. Recently, through a combination of neutron diffraction, quasi-elastic neutron scattering, nuclear magnetic resonance spin-lattice relaxation measurements, *ab initio* molecular dynamics simulations, and other techniques, dynamic motion has been observed in thiophosphate (PS_4^{3-}) [28, 29, 30, 31], hydroxide (OH^-) [32, 33, 34], borohydride (BH_4^-) [35], and closo-borate and derivative ($B_{10}H_{10}^{2-}$, $B_{12}H_{12}^{2-}$, etc.) [36, 37, 38] cluster anions. In some systems, anion rotation is restricted at lower temperatures and occurs only in high temperature phases [33, 38, 39]. In another, the partial substitution of a "faster" paddle-wheel (SiS_4^{4-}) for a "slower" one (PS_4^{3-}) has been correlated with increased lithium transport [31]. A more thorough understanding of the generalizable conditions that are amenable to cluster anion rotation, as well as specific interactions between cluster anions and working cations, is therefore highly desirable. In addition, a small number of known systems have more than one type of cluster anion, raising the possibility of diverse modes of correlated motion between multiple paddle-wheels and translating cations. That is the particular focus of

the present work, in which we consider sodium conduction in the double paddle-wheel system sodium amide borohydride ($Na_2(NH_2)(BH_4)$) and related compositions.

Like many metal borohydride compounds, sodium amide borohydride was initially considered for its hydrogen storage potential [40, 41] before garnering interest as a solid-state ion conductor due to its high sodium ion conductivity [42]. Multiple studies confirm the existence of a low-temperature orthorhombic phase (*Pbcm*) and a higher-temperature cubic phase (*Pm$\bar{}$3m*), although the phase transition temperature varies between accounts [41, 42]. A nuclear magnetic resonance study by Soloninin et al. [43] showed evidence of two separate hydrogen jump processes within the high temperature cubic phase, but did not attribute the hydrogen motion to the rotation of a specific anion. In the cubic phase, sodium amide borohydride assumes an antiperovskite structure (Figure 1A). Antiperovskites are an attractive model system with which to study paddle-wheel effects because, like perovskites, they are able to accommodate a diverse set of ionic substitutions, including multiple cluster anions. In this work we consider the single paddle-wheel antiperovskite sodium oxide borohydride ($Na_3O(BH_4)$) as one endmember of a series of compositions in which an increasing fraction *x* of the oxide (O^{2-}) anions are replaced by amide (NH_2^-) cluster anions. Charge balance mandates that each substitution is accompanied by a cation vacancy, resulting in sodium oxide amide borohydride ($Na_{3-x}O_{1-x}(NH_2)_x(BH_4)$). The fully substituted *x* = 1 composition is sodium amide borohydride ($Na_2(NH_2)(BH_4)$), in which $\frac{1}{3}$ of the sodium cation sites are vacant. As we show, this family of compositions exhibits an unusual positive deviation in ionic conductivity from the classical vacancy-dependent model with increasing concentrations of the second cluster anion, NH_2^-. The absolute conductivity of the *x* = 0 $Na_3O(BH_4)$ composition varies widely between literature reports, from 4.24×10^{-3} [26] to 2.46×10^{-10} S/cm [44], at room temperature. At the other end of the compositional series, the absolute conductivity of $Na_2(NH_2)(BH_4)$ is nearly identical to that of the well-known lithium-conducting antiperovskite, $Li_2(OH)Cl$ (Figure 1C and S5), ranging from 10^{-5} to 10^{-2} S/cm over the temperature range 50-200 °C [42], and is amongst the highest of known sodium antiperovskites. *Ab initio* molecular dynamics simulations (AIMD), X-ray and neutron diffraction, and solid state nuclear magnetic resonance (NMR) spectroscopy are used to reveal the temperature-dependent dynamics of both anion groups and their effects on sodium cation transport. We show that while there is a unique interaction of each cluster anion with the mobile cation, and with each other, rotational mobility of both anion groups is necessary for fast cation diffusion, providing the first clear example of a double paddle-wheel cation migration mechanism.

Anomalous Ionic Conductivity in $Na_2(NH_2)(BH_4)$

Across the series of $Na_{3-x}O_{1-x}(NH_2)_x(BH_4)$ compositions, PXRD measurements showed that the main phase (Rietveld refinement phase purity of > 99 wt%) is the cubic antiperovskite (space group *Pm$\bar{}$3m*) (Figure S1 and S2). As the substitution fraction *x* increases, the lattice parameter also increases linearly, indicating a continuous solid solution across the range of compositions studied. In the setting presented in Figure 1A, the borohydride cluster anions occupy the cubic vertex sites, the oxide/amide anions occupy the body center site, and the sodium cations occupy the face center sites, forming an octahedron. Charge balance mandates that each

substitution of an oxide anion for an amide is accompanied by a sodium cation vacancy, resulting in the stoichiometry $Na_{3-x}O_{1-x}(NH_2)_x(BH_4)$. At the $x = 1$ limiting composition $Na_2(NH_2)(BH_4)$, two of the octahedral sites are vacant and all body center sites contain amide cluster anions.

The temperature-dependent ionic conductivities of $Na_{3-x}O_{1-x}(NH_2)_x(BH_4)$ for $x = 0, 0.2, 0.5, 0.75$, and 1.0 were measured using AC impedance (Figure S3). DC polarization was performed to verify that the contribution of electronic conductivity is negligible for $Na_2(NH_2)(BH_4)$ (Figure S4), confirming an ionic transference number of unity. Figure 1B shows that the temperature-dependent conductivity of all $Na_{3-x}O_{1-x}(NH_2)_x(BH_4)$ compositions studied is linear in an Arrhenius plot above room temperature, indicating a single activated process. Though these measurements alone appear conventional, when the ionic conductivity is plotted against sodium vacancy concentration (Figure 1C), positive deviation from the predictions of a vacancy model (see Methods) is observed for cation vacancy concentrations greater than about 15% ($x = 0.5$), ultimately reaching values 10^2 greater than the extrapolated conductivity at $x = 1$. Clearly, the increase in vacancy concentration is not solely responsible for the increase in conductivity across the compositions.

SXRD and NPD Analysis

To better resolve the cubic antiperovskite structure, high-resolution synchrotron PXRD (SXRD) measurements were performed on $Na_2(NH_2)(BH_4)$ across a range of temperatures. Above 15 $^\circ$C, $Na_2(NH_2)(BH_4)$ maintains a cubic ($Pm\bar{3}m$) structure with a lattice parameter of 4.70 $^\circ$A at 15 $^\circ$C. In the setting presented in this paper, a typical cubic antiperovskite X_3AB would have X sites at $(\frac{1}{2}, \frac{1}{2}, 0)$, $(\frac{1}{2}, 0, \frac{1}{2})$, and $(0, \frac{1}{2}, \frac{1}{2})$, an A site at $(\frac{1}{2}, \frac{1}{2}, \frac{1}{2})$, and a B site at $(0, 0, 0)$. In the case of $Na_2(NH_2)(BH_4)$, Rietveld refinement of the SXRD shows four disordered sodium ion sites centered around each of these idealized posi-

tions. This could be a reflection of the high sodium mobility or evidence of octahedral tilting commonly found in perovskites and antiperovskites [45].

To determine the positions of the lighter hydrogen atoms with more precision, neutron powder diffraction (NPD) was performed on the isotopic variant $Na_2(NH_2)(^{11}BD_4)$. Again, the cubic ($Pm\bar{3}m$) structure was found, with a lattice parameter of 4.69410(4) $^\circ$A at 15 $^\circ$C, however the cubic to orthorhombic phase transition temperature was depressed to 0 $^\circ$C. Rietveld refinement from the diffraction pattern confirmed that the hydrogen and deuterium atoms do not significantly exchange positions during the synthesis process. In the cubic phase, Rietveld refinement and MEM analysis showed highly disordered, sphere-like arrangements of hydrogen and deuterium around their central nitrogen and boron atoms respectively. Such an arrangement could come from two types of disorder in the angular position of the cluster anions: (1) spatial disorder, in which the cluster anions are static but each arranged in a different angular position, so that averaging over the length scale of the measurement gives a spherical distribution of rotor atom positions, and (2) temporal disorder, in which the cluster anions are rotating faster than the time scale of the measurement, resulting in the same disordered distribution. While diffraction measurements alone cannot distinguish between these underlying causes, other techniques

discussed in later sections confirm the rotational motion of the cluster anions as the source of the distributed rotor atom positions.

At first glance, the atomic positions in the cubic and orthorhombic structures produced by SXRD analysis appear quite similar. However, there are two noticeable features in the orthorhombic phase that break the cubic symmetry. The first is a common phenomenon in both perovskites and antiperovskites: the tilting of the sodium octahedra. The next feature is more unique to $Na_2(NH_2)(BH_4)$ and likely has a large impact on the conductivity: Na/vacancy ordering. In the cubic phase, the sodium sites are identical by symmetry, so the vacancies are distributed equally over all sodium sites. These vacancies are disordered, at least on the time and length scales of the SXRD measurement. In the orthorhombic structure, the vacancies settle into positions specified in Figure 2B, becoming ordered. The result of this ordering, which precludes sodium vacancies from certain sites, is that cation diffusion in the orthorhombic structure has to rely on thermally generated vacancies on the high sodium occupancy sites (or a different diffusion mechanism altogether), resulting in lower conductivity. Furthermore, NPD analysis shows that the rotor atom positions become much more ordered in the transformation from cubic to orthorhombic structure, settling into the clearly identifiable shapes of the respective anions (tetrahedral for the borodeuteride and bent for the amide). This change in anion dynamics could also be responsible for a decrease in conductivity by way of the paddle-wheel effect. Here, we do not attempt to quantify the contribution of each mechanism to the experimentally observed two-order-of-magnitude decrease in conductivity that accompanies the cubic-to-orthorhombic phase transition. Instead, we focus on probing the effects of anion rotational dynamics on cation transport within the cubic phase, leaving the details of the orthorhombic phase to future work. While the diffraction techniques discussed give us valuable information about average atomic positions, we turned to AIMD to look for correlations between anion rotational and cation translational trajectories.

AIMD Analysis

In order to capture behavior over the experimental range of compositions and temperatures, AIMD simulations were conducted for $Na_{3-x}O_{1-x}(NH_2)_x(BH_4)$ at $x = 0$, 0.5, and 1, and each at temperatures of 250, 300, 363, 500, and 700 K. Diffusivities and probability density iso-surfaces generated by AIMD matched well with EIS and MEM analysis of neutron diffraction data (Figure S6 and S7). The sodium mean squared displacement (MSD), plotted against time in Figure 3C, is a direct reflection of the cation diffusivity and tracks with the experimental data: As the substitution of amide for oxide increases, the sodium MSD increases as well. The cluster anion rotational autocorrelation decay functions (plotted against time in Figure 3A and B) express the degree to which the orientation, u, of a cluster anion at time t is correlated to its initial orientation at $t = 0$, and is averaged across all anions of the same species:

$$C(t) = <u(t) \cdot u(t = 0)>$$

The rate at which this function decays to zero reflects the reorientation rate of that species. Figure 3A and B show that the amide rotation is more sensitive to changes in the composition; as the amide substitution fraction increases, its rate of rotation does as well. Meanwhile,

borohydride rotation is insensitive to the substitution fraction and is significantly faster than amide rotation as evidenced by the faster decay of its rotational autocorrelation function.

Individual sodium migration events were inspected in the $Na_2(NH_2)(BH_4)$ simulation at 363 K (Figure S8), tracking the translation of the sodium cation alongside the angular displacement of the neighboring cluster anions (Figure 4 and S9). A clear pattern is observed for all migration events, in which the neighboring amide cluster anions reorient in concert with the sodium ion as it moves from one lattice site to the next. In contrast, the local borohydride anions do not show the same synchronous behavior, and are rotating much faster than the amide anions. Despite this apparent lack of interaction between the borohydride anions and sodium cations, further simulations showed a more nuanced relationship between the ionic species.

To probe the interdependencies of the motional processes of each of the three ionic species (Na^+, NH_2 and BH_4^-) on the other two, simulations were run in which one species was frozen, and the effect of this constraint on the motion of the remaining two species was observed. Freezing the borohydride anions slowed the rotation of amide anions (Figure 3E), but completely quenched the translation of sodium cations (Figure 3F). Freezing the amide anions did not affect the rotation of the borohydride anions (Figure 3D), but again, completely quenched the translation of the sodium cations (Figure 3F). These simulations confirm the existence of a double paddle-wheel effect: The rotation of both cluster anions is necessary in order to enable a higher cation diffusivity, and the freezing of either one is sufficient to prevent fast cation migration. Next, we observed the effect of sodium cation motion on cluster anion rotation. When we freeze the sodium cations, only a noticeable slowing of amide rotation is observed (Figure 3E), while there is negligible effect on the rotation of the borohydride anions (Figure 3D).

Thus the pairwise interactions between the three species differ considerably. Amide anion rotational displacement is highly *synchronized* with the sodium cation migration; in every migration event, sodium ion displacement occurs simultaneously with amide rotation in the time domain (Figure 4 and S9). The correlation is also *symmetric*; freezing the amide anions slows the translation of the sodium cations, and vice versa. In contrast, the correlation between sodium cation translation and borohydride anion rotation is neither synchronous nor symmetric. The synchronized motion of sodium cations and amide anions is reasonable given their spatial proximity (sodium-nitrogen distance of 2.33 ˚A, sodium-hydrogen distance of 1.26 ˚A compared to the borohydride anion: sodium-boron distance of 3.30 ˚A and sodiumnitrogen distance of 2.05 ˚A). The indirect (but strong) effect of borohydride rotation on sodium ion translation may therefore occur by way of permitting amide rotation. The correlation between rotation of the two cluster anions is also neither synchronized nor symmetric; the borohydride rotates much faster, and freezing its motion slows rotation of the amide, but not vice versa.

NMR Analysis

In order to probe the sodium ion conductivity mechanism at the local level and understand the disparate influences of the cluster anions on the paddle-wheel motion, static [1]Na and [11]B

variable-temperature NMR measurements of the high-conductivity end-member $Na_2(NH_2)(BH_4)$ were recorded. Acquisition of these two nuclei proved experimentally straightforward and provided the most informative spectra. The static ^{23}Na variable-temperature NMR spectra of $Na_2(NH_2)(BH_4)$, depicted in Figure S11, show a highly temperature-dependent series of broad lineshapes that clearly indicate the onset and thermallyactivated increase of sodium ion motion. In particular, the spectrum at 15 °C (cubic phase) clearly displays one sodium site, with a typical quadrupolar lineshape ([23]Na is quadrupolar with spin I = 3/2) that consists of two well-separated shoulders. As the temperature increases, the linewidth of this feature significantly narrows, indicating effective averaging of the quadrupolar interaction due to rapid sodium ion motion. ^{23}Na NMR reveals clear evidence of the phase transition occurring between 15 °C and 10 °C on cooling, in which a second quadrupolar-broadened [23]Na site appears (Figure S11). No significant spectral changes are observed below the phase transition, indicating freezing out of the high-temperature sodium ion motion. The significant decrease in the sodium ion conductivity of the orthorhombic phase is thus directly correlated with the vacancy ordering and decrease in motional correlation time of the sodium ion hopping process (Figure 5C). This result shows that the conductivity decrease is tied to the structural rearrangement and vacancy ordering of the orthorhombic phase, in agreement with the SXRD results.

We performed saturation-recovery measurements of the [23]Na spin-lattice (T_1) relaxation times, which show a significant discontinuous increase at the phase transition (Figure 5A and B). Using the BPP theory [46], and applying the quadrupolar parameters obtained from fitting the [23]Na spectrum that were confirmed by DFT calculations (Figure S10), we could calculate motional correlation times τ_c at each temperature [47]. The τ_c values in the high-temperature cubic phase are thermally activated and can be fitted to an Arrhenius equation over the studied temperature range. We extract an activation energy E_a = 450 meV for the sodium ion hopping process in cubic $Na_2(NH_2)(BH_4)$, which is in reasonable agreement with high-temperature conductivity data (E_a = 552 meV for results in Figure 1B). This result corroborates the claim that the ^{23}Na NMR spectra report on the local mechanism of cation migration that leads to the high sodium ion conductivity.

In contrast to the ^{23}Na spectra, the ^{11}B NMR spectra show minimal change as a function of temperature even above and below the phase transition (Figure S11). As discussed below, the motional correlation times for [11]B, which can be ascribed to borohydride rotational and reorientational motion, are roughly an order of magnitude shorter than the corresponding values for sodium ion migration. This rapid rotational motion faster than the NMR spectral timescale makes the [11]B spectra relatively insensitive to motional changes. Moreover, the lack of clear change upon transition to the orthorhombic structure corroborates the AIMD result that freezing the cation motion has minimal impact on the borohydride autocorrelation function (Figure 3D).

We also measured [11]B spin-lattice (T_1) relaxation times (Figure 5C and D), and could apply the BPP formalism to the data where the [11]B quadrupolar parameters were taken from DFT-calculated values, as these could not be extracted directly from the spectra. The motional correlation times τ_c increase from 1 µs at 60 °C (a motional frequency of τ_c^{-1} = 1 MHz) to 7 µs at 15 °C (τ_c^{-1} = 140 kHz). Fitting an Arrhenius equation to the τ_c values in the cubic phase yields E_a = 400 meV, which is not dissimilar from that of sodium hopping (E_a = 450 meV) and the ion conductivity (E_a =

552 meV). This result demonstrates that although the timescales of the sodium migration and borohydride reorientation are significantly different, they possess similar activation energies for their respective motion, in agreement with a double paddle-wheel mechanism.

Conclusions

We observe that the cluster anion substituted cubic antiperovskite $Na_{3-x}O_{1-x}(NH_2)_x(BH_4)$ displays a large increase in ionic conductivity with substitution fraction x that cannot be explained by increasing vacancy concentration alone. We investigate the possibility of a double paddle-wheel mechanism as an explanation for this behavior, using X-ray scattering, neutron scattering, NMR, electrical conductivity measurements conducted between (-5) – 30 °C, and AIMD simulations for temperatures between (-23) – 427 °C (250 – 700 K). For the cubic phase, the spatial probability density iso-surfaces of hydrogen atoms associated with both cluster anions forms lobed spheres in excellent agreement with AIMD simulations. Additionally, NMR spectra show quadrupolar coupling constants that agree well with DFT calculations while spin-lattice relaxation measurements suggest rotational motion of the borohydride anions that is also consistent with AIMD simulations. These simulations allow us to look more closely at the rotational behavior of each cluster anion and its impact on sodium ion mobility. We found that while the borohydride anions rotate faster than the amide anions, only the rotation of the amide anions is closely synchronized with the translation of sodium ions during migration events. Selective freezing simulations showed an asymmetric relationship between the borohydride and sodium ions but a symmetric relationship between the amide and sodium ions, while confirming that rotational activity of both anions is required to enable high sodium ion mobility. In the context of solid ion conductors, a paddle-wheel effect is said to exist when the rotational dynamics of a complex anion facilitate the mobility of a cation. In the present amide-borohydride system, the synchronous correlations observed between NH_2^- reorientations and Na^+ migration is consistent with this definition. However, the present system also exhibits indirect correlations between BH_4^- anions and Na^+ cations that operate via the NH_2^- anions. This latter phenomenon, which is reported here for the first time, may be considered as an "indirect paddle-wheel effect." Given that the rotational behavior of both the amide and borohydride groups influence cation mobility (albeit distinctly), we designate $Na_2(NH_2)(BH_4)$ as a "double paddle-wheel" system. Upon cooling of the cubic phase below 10 °C, a transition to an orthorhombic phase (x = 1 composition) is observed in which cation vacancies are ordered and the rotational mobility of the cluster anions is severely limited, and correspondingly, the sodium conductivity decreases by about a factor of 10^2.

Methods

To avoid uncontrolled interactions with air and water vapor, all of the following procedures were carried out in argon-filled gloveboxes or containers with < 1 ppm O_2 and < 1 ppm H_2O unless otherwise specified.

Materials Synthesis

A series of compositions $Na_{3-x}O_{1-x}(NH_2)_x(BH_4)$ (x = 0, 0.2, 0.5, 0.75, 1.0) as well as $Na_2(NH_2)(^{11}BD_4)$ were prepared through solid-state reaction using Na_2O (Sigma-Aldrich, anhydrous, 80% Na_2O and 20% Na_2O_2), $NaNH_2$ (Fisher Scientific, anhydrous, 99%), $NaBH_4$ (Sigma-Aldrich, anhydrous, 99.99%), and $Na^{11}BD_4$ (Katchem, anhydrous, 98%). 4 g of the reactants were mixed and ground for $\frac{1}{2}$ to 1 hour in a high-energy ball mill (SPEX SamplePrep Mixer/Mill 8000 M) using a steel jar and steel milling balls (2 balls of $\frac{1}{4}$ inch diameter and 2 of $\frac{1}{2}$ inch diameter), and then hydraulically pressed in a $\frac{1}{2}$ inch diameter die at 60 MPa for 2 min to form disc-shaped pellets. The pressed pellets were heat treated for 24 hours at temperatures ranging from 100 to 250 °C depending on the composition (specific temperatures listed in Table S1), then polished to remove surface impurities. Powder for analysis was obtained by hand grinding the resultant pellets using an agate mortar and pestle.

Electrical Conductivity Measurements

Blocking electrodes were formed by sputtering gold onto both polished faces of 1 mm thick pellets using a sputter coater (Cressington Scientific Instruments 108 Manual). Impedance spectroscopy measurements were performed over the frequency range 50 mHz to 1 MHz with amplitude 100 mV, over a temperature range of (-20) - 240 °C using BioLogic VMP3 impedance analyzers. A temperature ramp rate of 0.16 °C/min and soak time of 30 min were used. An equivalent circuit was used to fit the real and imaginary components of the AC impedance, which showed a single semi-circle. Direct current polarization was also performed over a temperature range of 40 - 100 °C using a bias of 100 mV applied for 1 to 5 min.

Differential Scanning Calorimetry (DSC)

Samples were sealed inside hermetic aluminum pans. DSC measurements were performed using the TA Instruments DSC Q100 instrument over a temperature range of (-100) - 50 °C at temperature scan rates of 2 °C/min, 5 °C/min, and 10 °C/min.

X-ray Diffraction (XRD)

The crystalline phases were characterized by powder X-ray diffraction (PXRD), using a PANalytical X'Pert Pro multipurpose diffractometer equipped with a Cu Kα radiation source and an X'Celerator detector. For temperature-dependent XRD over (-20) - 25 °C, a ramp rate of 5 °C/min, soak time of 30 min, and scan time of 24 min were used.

Synchrotron X-ray Diffraction (SXRD)

High-resolution SXRD data was collected using the high-resolution powder diffraction beamline 11-BM at the Advanced Photon Source (APS) of Argonne National Laboratory at an energy of 27 keV. The $Na_2(NH_2)(BH_4)$ and $Na_2(NH_2)(^{11}BD_4)$ powder samples were loaded in 1 mm diameter quartz capillaries and sealed with epoxy. Data was collected at temperatures in the range of (-100) - 30 °C.

Nuclear Magnetic Resonance Spectroscopy (NMR)

Static ^{23}Na and ^{11}B NMR measurements were primarily performed at a field strength of 11.7 T corresponding to Larmor frequencies of 132.32 MHz and 160.49 MHz, respectively, using a 500 MHz Bruker Avance I spectrometer and a Bruker 5 mm double-resonance broadband observe (BBO) probe equipped with variable-temperature control (additional ^{23}Na NMR experiments were performed at a field strength of 16.4 T corresponding to a Larmor frequency of 185.19 MHz, using a 700 MHz Bruker Avance I spectrometer and a Bruker 5 mm BBO probe; see Figure S10). Experiments were performed on $Na_2(NH_2)(BH_4)$ samples that had been previously flame-sealed in 5 mm NMR tubes under an inert atmosphere in order to limit air and moisture exposure. Typical RF pulse lengths were 2.2 μs for [23]Na (corresponding to a $\frac{\pi}{4}$ pulse for the [23]Na reference, to account for quadrupolar nutation effects [48]) and 13 μs for [11]B. [23]Na shifts were referenced to 1 M NaCl (aq) at 0 ppm, and [11]B shifts were referenced to 0.1 M $B(OH)_3$ (aq) at 20 ppm. Temperature calibration was performed by measuring the known temperature-dependent difference of the ^{1}H chemical shifts of the –C**H**2– and –O**H** resonances of dry ethylene glycol [49]. Samples were allowed to equilibrate at the measurement temperature for 15 min prior to acquisition of spectra. Data were acquired, processed and analyzed using Bruker TopSpin 2.1 and/or 3.6.

Neutron Diffraction

Time-of-flight neutron diffraction data was collected at the NOMAD instrument at the Spallation Neutron Source (SNS) at Oak Ridge National Laboratory (ORNL). About 0.3 g of $Na_2(NH_2)(^{11}BD_4)$ was loaded into 3 mm diameter quartz capillaries and sealed under Ar atmosphere with epoxy resin. The data was collected between 100 and 303 K with neutron wavelength band widths of 0.1 – 3.0 ˚A. Timeof-flight (TOF) was converted to d-spacing using the conventional second order polynomial

$$TOF = ZERO + DIFC \cdot d + DIFA \cdot d^2$$

where *ZERO* is a constant, *DIFC* is the diffractometer constant and *DIFA* is an empirical term to correct for sample displacements and absorption induced peak shifts. *ZERO* and *DIFC* were determined from the refinement of a standard NIST Si-640e data set and held fixed, while *DIFA* was allowed to vary during refinements to account for the sample displacements. For the low-resolution frames (bank 2 and 3), a back-to-back exponential function convoluted with a symmetrical Gaussian function was used to describe the peak profile. For the high-resolution frames (bank 4 and 5), the moderator induced line profile was modeled using a modified Ikeda-Carpenter-David function [50, 51]. The Lorenz factor was accounted for by multiplying (d^4) [52]. Absorption correction was carried out using the empirical Lobanov formula.

Maximum Entropy Method Analysis

The distribution of nuclear density in in $Na_2(NH_2)(^{11}BD_4)$ was analyzed using maximum entropy method (MEM) with Dysnomia [53]. The input file (.mem) for MEM analysis was generated by loading the NPD data in Jana2006 [54], and the output file (.pgrid) generated by Dysnomia was examined in VESTA [55].

Density Functional Theory (DFT)

Calculations were performed with the Vienna ab initio simulation package (VASP) [56]. Core-valence electron interactions were treated with the projector-augmented wave method [57, 58]. The generalized gradient approximation in the formulation of Perdew-Burke-Ernzerhof was used for exchange and correlation [59]. The plane-wave cutoff energy was set to 550 eV. The energy criterion for convergence of the self-consistency loop was set to 10^{-5} eV, and the force criterion for the relaxation of geometric degrees of freedom (ion positions and cell geometry) was 0.01 eV/°A. The orthorhombic (*Pbcm*) unit cell of $Na_2(NH_2)(BH_4)$ was generated using the experimental atomic structures with H atoms positioned at the highest occupancies around B and N atoms to model BH_4^- and NH_2^-. A 4 × 4 × 3 k-point mesh was used for the orthorhombic unit cell.

For NMR calculations, finer DFT settings were used. These include a cutoff energy of 800 eV, a convergence criterion for the self-consistency loop of 10^{-8} eV, and a 6 × 6 × 4 k-point mesh for the orthorhombic (*Pbcm*) unit cell of $Na_2(NH_2)(BH_4)$. To simulate the quadrupolar interaction for NMR spectroscopy, the electric field gradient (EFG) tensors were calculated using the method by Petrilli et al. as implemented in VASP [60]. The asymmetry parameter (η_Q) was calculated from the principal components of the symmetrized EFG tensor (*V*), where by convention $|V_{zz}| > |V_{xx}| > |V_{yy}|$ and $0 \le \eta_Q \le 1$ [61]:

$$\eta_Q = \frac{|V_{xx} - V_{yy}|}{|V_{zz}|}$$

The quadrupolar coupling constants (C_Q) were calculated from the electron charge (*e*), the nuclear electric quadrupole moment (*Q*) (40.59, 20.44, and 104 millibarns for ^{11}B, ^{14}N, and ^{23}Na, respectively) [62], and Planck's constant (*h*) [61]:

$$C_Q = \frac{eQV_{zz}}{h}$$

Ab-initio Molecular Dynamics (AIMD)

Simulations were carried out using computational cells constructed from 3 × 3 × 3 replications of the cubic ($Pm\bar{3}m$) unit cell with composition $Na_{3-x}O_{1-x}(NH_2)_x(BH_4)$, where $x = 0, 0.5, 1$. The supercells of $Na_{3-x}O_{1-x}(NH_2)_x(BH_4)$ with $x = 0.5$ and 1 were modeled by replacing O atoms by NH_2 molecules and removing Na atoms randomly from the 3 × 3 × 3 supercell of $Na_3O(BH_4)$ (i.e. $x = 0$) according to the stoichiometry. A 2 × 2 × 1 supercell was used to simulate the orthorhombic (*Pbcm*) phase; in this case a single composition ($x = 1$) was employed. A Gamma-only k-point mesh was used and the plane-wave cutoff energy was set to 500 eV. For temperatures ranging from 250 K to 700 K, a minimum duration of 50 ps of dynamics was collected after an initial 3 ps of equilibration. Parrinello-Rahman dynamics were employed in combination with a Langevin thermostat [63, 64]. The friction coefficient for atomic species and the lattice was 10 ps^{-1}, the lattice mass was set to 1000 amu, and the MD time step was 0.5 femtoseconds.

Vacancy Diffusion Mechanism Model

A classical vacancy-dependent model of diffusion was used to relate the diffusion and ionic conductivity to the sodium ion vacancy concentration. The following equations relate the diffusion coefficient for the sodium ion (*D*) and the vacancy (D_v) to the number of adjacent sites

(z), attempt frequency (ν_0), jump distance (a_0), energy barrier to migration (ΔG_m), fractional concentration of the sodium ion (c), correlation factor (f), Boltzmann's constant (k), and temperature (T):

$$D_v = \frac{z\nu_0 a_0^2}{6} \exp\left(\frac{-\Delta G_m}{kT}\right)$$

$$D = (1-c)D_v f$$

Conductivity (σ) and diffusivity are related via site concentration (N), charge (q), and mobility (μ) as described by the Nernst-Einstein relation:

$$\sigma = Ncq\mu$$

$$D = \frac{\mu kT}{q}$$

$$\sigma = \frac{Ncq^2}{kT}D$$

This yields the following relationship between conductivity and vacancy concentration seen in Figure 1C:

$$\sigma = \frac{q^2 z}{6kT} Nc(1-c)fa_0^2\nu_0 \exp\left(\frac{-\Delta G_m}{kT}\right)$$

Terms that are not explicitly dependent on vacancy concentration or temperature are grouped into parameters A and B, which are then fit to the conductivity data.

$$\log\sigma = A + \log\left[c(1-c)\right] - \log\sigma_0 - \frac{B}{T}$$

Note that site concentration is inversely proportional to the cube of the lattice parameter. Because variables such as the correlation factor and attempt frequency may have unknown temperature dependence, the fitted parameter B cannot be directly interpreted as $\frac{\Delta G_m}{k}$.

Supporting Information

Supporting Information is available from the Wiley Online Library or from the author.

Acknowledgements

References

[1] J. B. Goodenough, K.-S. Park, *Journal of the American Chemical Society* **2013**, *135*, 4 1167, publisher: American Chemical Society.

[2] M. A. Laguna-Bercero, *Journal of Power Sources* **2012**, *203* 4.

[3] N. Mahato, A. Banerjee, A. Gupta, S. Omar, K. Balani, *Progress in Materials Science* **2015**, *72* 141.

[4] R. Ayers, *Journal of Industrial Ecology* **1997**, *1*, 1 81, _eprint: https://onlinelibrary.wiley.com/doi/pdf/10.1162/jiec.1997.1.1.81.

[5] H. Kvande, P. A. Drabløs, *Journal of Occupational and Environmental Medicine* **2014**, *56*, 5 Suppl S23.

[6] P. Knauth, *Solid State Ionics* **2009**, *180*, 14 911.

[7] J. Janek, W. G. Zeier, *Nature Energy* **2016**, *1*, 9 1, number: 9 Publisher: Nature Publishing Group.

[8] J. F. M. Oudenhoven, L. Baggetto, P. H. L. Notten, *Advanced Energy Materials* **2011**, *1*, 1 10, eprint: https://onlinelibrary.wiley.com/doi/pdf/10.1002/aenm.201000002.

[9] A. Manthiram, X. Yu, S. Wang, *Nature Reviews Materials* **2017**, *2*, 4 1, bandiera abtest: a Cg type: Nature Research Journals Number: 4 Primary atype: Reviews Publisher: Nature Publishing Group Subject term: Batteries Subject _term id: batteries.

[10] K. L. Gering, *Electrochimica Acta* **2017**, *225* 175.

[11] N. Kamaya, K. Homma, Y. Yamakawa, M. Hirayama, R. Kanno, M. Yonemura, T. Kamiyama, Y. Kato, S. Hama, K. Kawamoto, A. Mitsui, *Nature Materials* **2011**, *10*, 9 682, number: 9 Publisher: Nature Publishing Group.

[12] X. He, Y. Zhu, Y. Mo, *Nature Communications* **2017**, *8*, 1 15893, bandiera abtest: a Cc license type: cc _by Cg _type: Nature Research Journals Number: 1 Primary atype: Research Publisher: Nature Publishing Group Subject term: Atomistic models;Materials for energy and catalysis Subject term id: atomistic-models;materials-for-energy-and-catalysis.

[13] J. C. Bachman, S. Muy, A. Grimaud, H.-H. Chang, N. Pour, S. F. Lux, O. Paschos, F. Maglia, S. Lupart, P. Lamp, L. Giordano, Y. Shao-Horn, *Chemical Reviews* **2016**, *116*, 1 140, publisher: American Chemical Society.

[14] Z. Zhang, Y. Shao, B. Lotsch, Y.-S. Hu, H. Li, J. Janek, L. F. Nazar, C.-W. Nan, J. Maier, M. Armand, L. Chen, *Energy & Environmental Science* **2018**, *11*, 8 1945, publisher: Royal Society of Chemistry.

[15] Z. Zhang, Z. Zou, K. Kaup, R. Xiao, S. Shi, M. Avdeev, Y.-S. Hu, D. Wang, B. He, H. Li, X. Huang, L. F. Nazar, L. Chen, *Advanced Energy Materials* **2019**, *9*, 42 1902373, eprint: https://onlinelibrary.wiley.com/doi/pdf/10.1002/aenm.201902373.

[16] Y. Wang, W. D. Richards, S. P. Ong, L. J. Miara, J. C. Kim, Y. Mo, G. Ceder, *Nature Materials* **2015**, *14*, 10 1026, number: 10 Publisher: Nature Publishing Group.

[17] M. A. Kraft, S. P. Culver, M. Calderon, F. Bo¨cher, T. Krauskopf, A. Senyshyn, C. Dietrich, A. Zevalkink, J. Janek, W. G. Zeier, *Journal of the American Chemical Society* **2017**, *139*, 31 10909, publisher: American Chemical Society.

[18] T. Krauskopf, C. Pompe, M. A. Kraft, W. G. Zeier, *Chemistry of Materials* **2017**, *29*, 20 8859, publisher: American Chemical Society.

[19] E. P. Ramos, Z. Zhang, A. Assoud, K. Kaup, F. Lal`ere, L. F. Nazar, *Chemistry of Materials* **2018**, *30*, 21 7413, publisher: American Chemical Society.

[20] R. Schlem, S. Muy, N. Prinz, A. Banik, Y. Shao-Horn, M. Zobel, W. G. Zeier, *Advanced Energy Materials* **2020**, *10*, 6 1903719, eprint: https://onlinelibrary.wiley.com/doi/pdf/10.1002/aenm.201903719.

[21] Z. Zhang, L. F. Nazar, *Nature Reviews Materials* **2022**, *7*, 5 389, number: 5 Publisher: Nature Publishing Group.

[22] M. Jansen, *Angewandte Chemie International Edition in English* **1991**, *30*, 12 1547, eprint: https://onlinelibrary.wiley.com/doi/pdf/10.1002/anie.199115471.

[23] L. Karlsson, R. L. McGreevy, *Solid State Ionics* **1995**, *76*, 3 301.

[24] D. Wilmer, K. Funke, M. Witschas, R. Banhatti, M. Jansen, G. Korus, J. Fitter, R. Lechner, *Physica B: Condensed Matter* **1999**, *266*, 1-2 60.

[25] Y. Wang, Q. Wang, Z. Liu, Z. Zhou, S. Li, J. Zhu, R. Zou, Y. Wang, J. Lin, Y. Zhao, *Journal of Power Sources* **2015**, *293* 735.

[26] Y. Sun, Y. Wang, X. Liang, Y. Xia, L. Peng, H. Jia, H. Li, L. Bai, J. Feng, H. Jiang, J. Xie, *Journal of the American Chemical Society* **2019**, *141*, 14 5640, publisher: American Chemical Society.

[27] J. G. Smith, D. J. Siegel, *Nature Communications* **2020**, *11*, 1 1483, number: 1 Publisher: Nature Publishing Group.

[28] I. Hanghofer, B. Gadermaier, H. M. R. Wilkening, *Chemistry of Materials* **2019**, *31*, 12 4591, publisher: American Chemical Society.

[29] T. Famprikis, J. A. Dawson, F. Fauth, O. Clemens, E. Suard, B. Fleutot, M. Courty, J.-N. Chotard, M. S. Islam, C. Masquelier, *ACS Materials Letters* **2019**, *1*, 6 641, publisher: American Chemical Society.

[30] Z. Zhang, P.-N. Roy, H. Li, M. Avdeev, L. F. Nazar, *Journal of the American Chemical Society* **2019**, *141*, 49 19360.

[31] Z. Zhang, H. Li, K. Kaup, L. Zhou, P.-N. Roy, L. F. Nazar, *Matter* **2020**, *2*, 6 1667.

[32] A.-Y. Song, K. Turcheniuk, J. Leisen, Y. Xiao, L. Meda, O. Borodin, G. Yushin, *Advanced Energy Materials* **2020**, *10*, 8 1903480, eprint: https://onlinelibrary.wiley.com/doi/pdf/10.1002/aenm.201903480.

[33] F. Wang, H. A. Evans, K. Kim, L. Yin, Y. Li, P.-C. Tsai, J. Liu, S. H. Lapidus, C. M. Brown, D. J. Siegel, Y.-M. Chiang, *Chemistry of Materials* **2020**, *32*, 19 8481, publisher: American Chemical Society.

[34] Z. Deng, M. Ou, J. Wan, S. Li, Y. Li, Y. Zhang, Z. Deng, J. Xu, Y. Qiu, Y. Liu, C. Fang, Q. Li, L. Huang, J. Zhu, S. Han, J. Han, Y. Zhao, *Chemistry of Materials* **2020**, *32*, 20 8827, publisher: American Chemical Society.

[35] T. Ikeshoji, E. Tsuchida, T. Morishita, K. Ikeda, M. Matsuo, Y. Kawazoe, S.-i. Orimo, *Physical Review B* **2011**, *83*, 14 144301, publisher: American Physical Society.

[36] N. Verdal, T. J. Udovic, V. Stavila, W. S. Tang, J. J. Rush, A. V. Skripov, *The Journal of Physical Chemistry C* **2014**, *118*, 31 17483, publisher: American Chemical Society.

[37] T. J. Udovic, M. Matsuo, W. S. Tang, H. Wu, V. Stavila, A. V. Soloninin, R. V. Skoryunov, O. A. Babanova, A. V. Skripov, J. J. Rush, A. Unemoto, H. Takamura, S.-i. Orimo, *Advanced Materials* **2014**, *26*, 45 7622, _eprint: https://onlinelibrary.wiley.com/doi/pdf/10.1002/adma.201403157.

[38] W. S. Tang, M. Dimitrievska, V. Stavila, W. Zhou, H. Wu, A. A. Talin, T. J. Udovic, *Chemistry of Materials* **2017**, *29*, 24 10496, publisher: American Chemical Society.

[39] D. Sveinbjo¨rnsson, J. S. G. Myrdal, D. Blanchard, J. J. Bentzen, T. Hirata, M. B. Mogensen, P. Norby, S.-I. Orimo, T. Vegge, *The Journal of Physical Chemistry C* **2013**, *117*, 7 3249, publisher: American Chemical Society.

[40] P. A. Chater, P. A. Anderson, J. W. Prendergast, A. Walton, V. S. J. Mann, D. Book, W. I. F. David, S. R. Johnson, P. P. Edwards, *Journal of Alloys and Compounds* **2007**, *446-447* 350.

[41] M. Somer, S. Acar, C. Koz, I. Kokal, P. Ho¨hn, R. Cardoso-Gil, U. Aydemir, L. Akselrud, *Journal of Alloys and Compounds* **2010**, *491*, 1 98.

[42] M. Matsuo, S. Kuromoto, T. Sato, H. Oguchi, H. Takamura, S.-i. Orimo, *Applied Physics Letters* **2012**, *100*, 20 203904, publisher: American Institute of Physics.

[43] A. V. Soloninin, O. A. Babanova, E. Y. Medvedev, A. V. Skripov, M. Matsuo, S.-i. Orimo, *The Journal of Physical Chemistry C* **2014**, *118*, 27 14805, publisher: American Chemical Society.

[44] E. Ahiavi, J. A. Dawson, U. Kudu, M. Courty, M. S. Islam, O. Clemens, C. Masquelier, T. Famprikis, *Journal of Power Sources* **2020**, *471* 228489.

[45] T.-L. Pham, A. Samad, H. J. Kim, Y.-H. Shin, *Journal of Applied Physics* **2018**, *124*, 16 164106, publisher: American Institute of Physics.

[46] N. Bloembergen, *Physical Review* **1956**, *104*, 6 1542, publisher: American Physical Society.

[47] S. Indris, P. Heitjans, R. Uecker, B. Roling, *The Journal of Physical Chemistry C* **2012**, *116*, 27 14243, publisher: American Chemical Society.

[48] A. P. M. Kentgens, *Geoderma* **1997**, *80*, 3 271.

[49] C. Ammann, P. Meier, A. Merbach, *Journal of Magnetic Resonance (1969)* **1982**, *46*, 2 319.

[50] S. Ikeda, J. M. Carpenter, *Nuclear Instruments and Methods in Physics Research Section A: Accelerators, Spectrometers, Detectors and Associated Equipment* **1985**, *239*, 3 536.

[51] J. Liu, Z. Du, X. Wang, S. Tan, X. Wu, L. Geng, B. Song, P.-H. Chien, S. M. Everett, E. Hu, *Energy & Environmental Science* **2021**, *14*, 12 6441.

[52] A. C. Larson, R. B. V. Dreele, GSAS: General Structure Analysis System. Rep. No. LA-UR-86748, **1994**.

[53] K. Momma, T. Ikeda, A. A. Belik, F. Izumi, *Powder Diffraction* **2013**, *28*, 3 184, publisher: Cambridge University Press.

[54] V. Petˇrˊiˇcek, M. Duˇsek, L. Palatinus, *Zeitschrift fu¨r Kristallographie - Crystalline Materials* **2014**, *229*, 5 345, publisher: Oldenbourg Wissenschaftsverlag.

[55] K. Momma, F. Izumi, *Journal of Applied Crystallography* **2008**, *41*, 3 653, number: 3 Publisher: International Union of Crystallography.

[56] G. Kresse, J. Furthmu¨ller, *Physical Review B* **1996**, *54*, 16 11169, publisher: American Physical Society.

[57] P. E. Blo¨chl, *Physical Review B* **1994**, *50*, 24 17953, publisher: American Physical Society.

[58] G. Kresse, D. Joubert, *Physical Review B* **1999**, *59*, 3 1758, publisher: American Physical Society.

[59] J. P. Perdew, K. Burke, M. Ernzerhof, *Physical Review Letters* **1996**, *77*, 18 3865, publisher: American Physical Society.

[60] H. M. Petrilli, P. E. Blo¨chl, P. Blaha, K. Schwarz, *Physical Review B* **1998**, *57*, 23 14690, publisher: American Physical Society.

[61] P. P. Man, In R. A. Meyers, editor, *Encyclopedia of Analytical Chemistry*, a6111. John Wiley & Sons, Ltd, Chichester, UK, ISBN 978-0-471-97670-7 978-0-470-02731-8, **2006**, URL https://onlinelibrary.wiley.com/doi/10.1002/9780470027318.a6111.

[62] P. Pyykk¨o, *Molecular Physics* **2008**, *106*, 16-18 1965, publisher: Taylor & Francis eprint: https://doi.org/10.1080/00268970802018367.

[63] M. Parrinello, A. Rahman, *Physical Review Letters* **1980**, *45*, 14 1196, publisher: American Physical Society.

[64] M. Parrinello, A. Rahman, *Journal of Applied Physics* **1981**, *52*, 12 7182, publisher: American Institute of Physics.
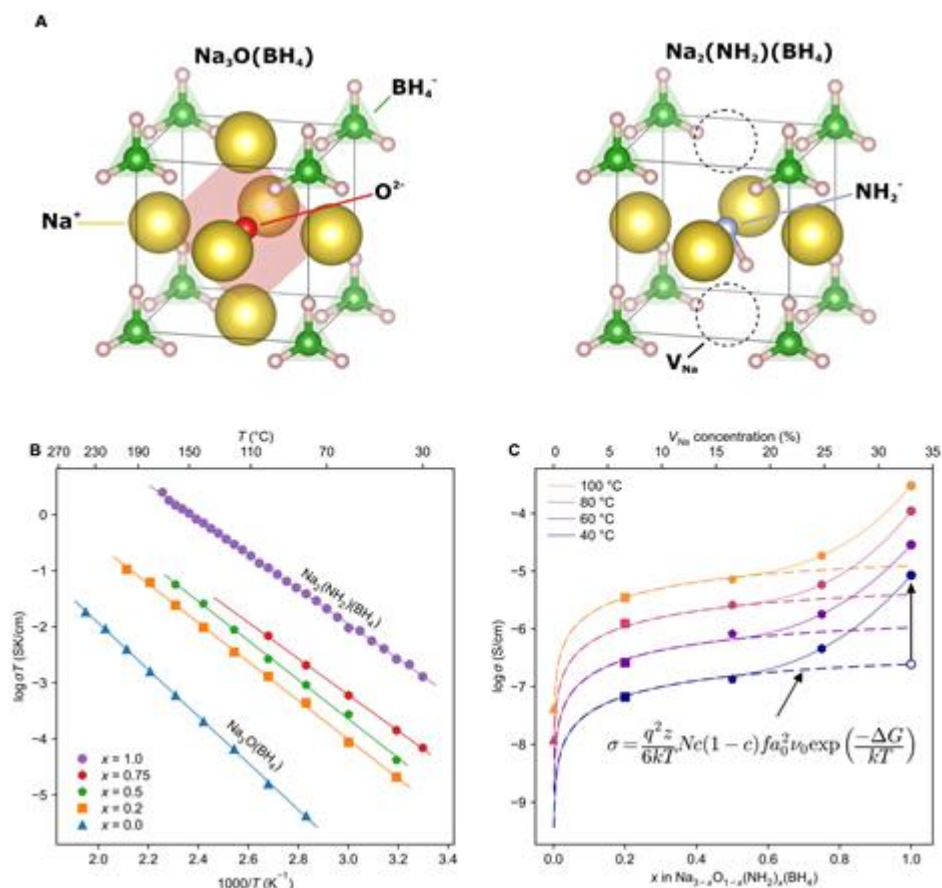
Figure 1 Sodium ion transport in $Na_{3-x}O_{1-x}(NH_2)_x(BH_4)$ ($x = 0 – 1$) upon systematic substitution of O^{2-} by NH_2^-, with corresponding increase in Na^+ vacancy concentration. (A) Powder X-ray diffraction (PXRD) shows that the whole series of compositions $Na_{3-x}O_{1-x}(NH_2)_x(BH_4)$ form cubic antiperovskites with space group $Pm\bar{3}m$ at room temperature (Figure S1). Between the endmember compositions $Na_3O(BH_4)$ and $Na_2(NH_2)(BH_4)$, the Na^+ vacancy concentration increases from zero to one-third at full substitution of O^{2-} by NH_2^-. In the cubic unit cell $Na_3O(BH_4)$ (A, left), Na^+ ions at the face-centered sites comprise the vertices of the Na_6O octahedra, and $(BH4-)$ cluster anions occupy the corner sites. In the cubic unit cell $Na_2(NH_2)(BH_4)$ (A, right), two of those the six Na^+ ions are missing, and the O^{2-} ion residing at the center of the pseudo-octahedron is replaced with an NH_2^- anion. (B) Temperature-dependent ionic conductivity of $Na_{3-x}O_{1-x}(NH_2)_x(BH_4)$ (where x = 0, 0.2, 0.5, 0.75, and 1.0) exhibits Arrhenius behavior above the room temperature region and ionic conductivity increases with the substitution of O^{2-} by NH_2^-. Activation energies are 0.358, 0.299, 0.301, 0.278, and 0.268 eV respectively. The endmember composition $Na_2(NH_2)(BH_4)$ with the highest Na^+ vacancy and NH_2^- cluster anion concentration shows 10^4 higher ionic conductivity than that of the endmember $Na_3O(BH_4)$ without the substitution of NH_2^-. (C) The dependence of ionic conductivity on the concentration of Na^+ vacancy and NH_2^- cluster ion concentration at several temperatures between 40 °C and 100 °C is fitted as the dashed line using the vacancy-dependent ionic conductivity model (inset equation). At low x (≤ 0.75), the ionic conductivity can be fit well by the classical vacancy-concentration model. At high x (> 0.75), ionic conductivity of $Na_{3-x}O_{1-x}(NH_2)_x(BH_4)$ exhibits a large positive deviation from the expected classical vacancy-dependent conductivity. It is correlated with not only high vacancy concentration but also the NH_2^- cluster anion concentration, suggesting a paddle-wheel effect.
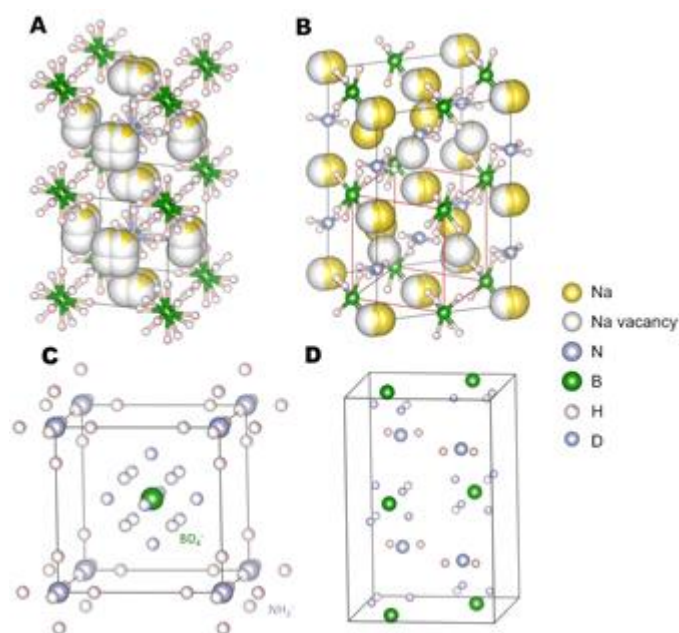
Figure 2 (A) Two vertically stacked $Na_2(NH_2)(BH_4)$ cubic unit cells and (B) one orthorhombic unit cell with corresponding cubic unit cell marked with red lines, from Rietveld refinement of synchrotron XRD data. The cubic phase exhibits greater vacancy and anion rotational disorder compared to the orthorhombic phase. (C) $Na_2(NH_2)(^{11}BD_4)$ cubic unit and (D) orthorhombic unit cells from Rietveld refinement of neutron diffraction data with sodium removed for clarity. Neutron diffraction is more sensitive to the light hydrogen and deuterium and confirms the increased ordering of anion orientation in the orthorhombic phase.
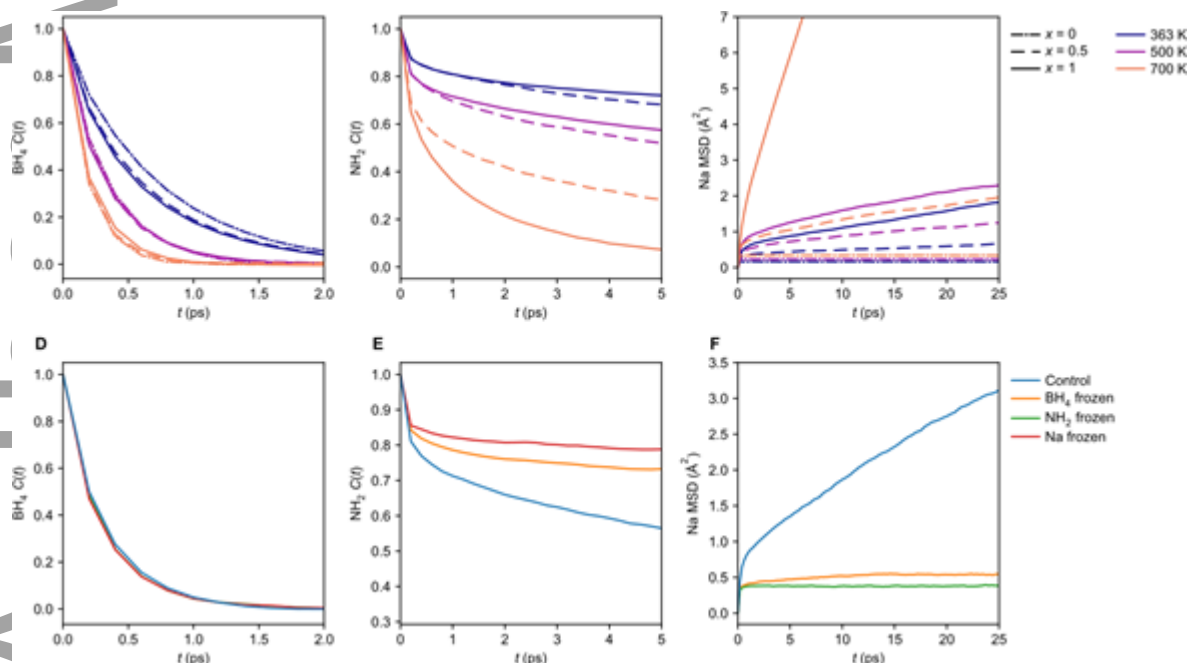

Figure 3 (A, D) Borohydride and (B, E) amide orientation autocorrelation functions and (C, F) sodium MSD. (A, B, and C) AIMD simulations of $Na_{3-x}O_{1-x}(NH_2)_x(BH_4)$ for x = 0, 0.5, 1 and T = 363, 500, and 700 K. Borohydride rotation is relatively unchanged throughout the anion substitution while amide rotation shows a strong speedup as the proportion of amide to oxide anion increases within the 700 K condition. (D, E, and F) Simulations of $Na_2(NH_2)(BH_4)$ with either sodium, amide, or

borohydride ions artificially frozen. Borohydride rotation remains insensitive to freezing of other ionic species, while the rates of amide rotation and sodium migration are slowed by any other ion freezing.
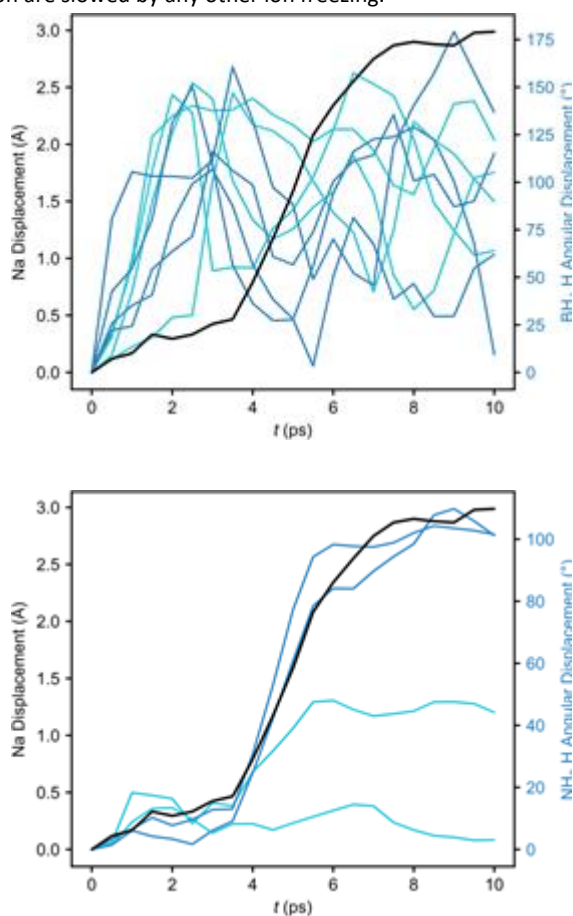

Figure 4 Correlation between sodium ion translation (left vertical axis, black line) and cluster anion angular displacement (right vertical axis, blue lines, the shade is indicative of which of the two nearest neighbors the hydrogen belongs to) plotted against time during a representative migration event in a 50 ps AIMD simulation of $Na_2(NH_2)(BH_4)$ at 363 K (for additional migration events see Figure S9 in the SI). (A) Amide rotation is slower but highly synchronized with sodium migration, while (B) borohydride rotation is faster but less synchronized.
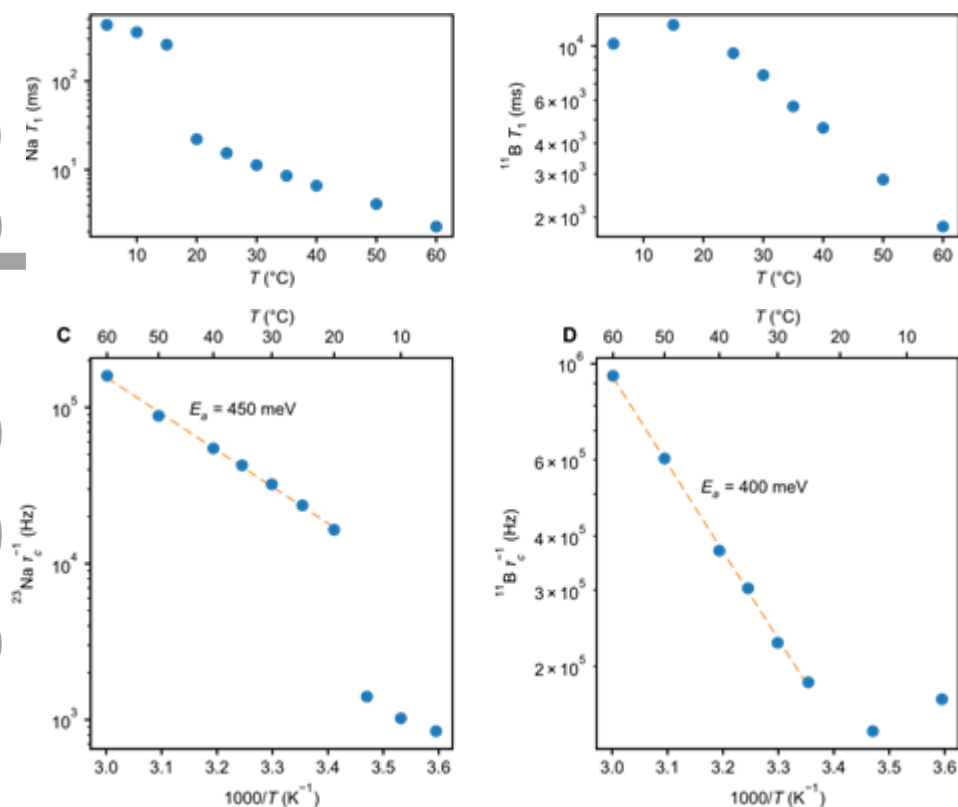
Figure 5 Experimental (A) ^{23}Na and (B) ^{11}B T_1 relaxation times of Na$_2$(NH$_2$)(BH$_4$) measured as a function of temperature; the phase transition is apparent as the sudden increase in ^{23}Na T_1. (C, D) Correlation times τ_c extracted from the T_1 values in (A) and (B) respectively, using the following equation derived from the BPP theory:

$$\frac{1}{T_1} = \frac{2\pi^2}{25} \cdot C_Q^2 \left(1 + \frac{1}{3}\eta_Q^2\right) \cdot \left[\frac{\tau_c}{1 + \frac{4\tau_c}{1+\omega_0^2\tau_c^2} + 4\omega_0^2\tau_c^2}\right]$$

For sodium, the values of the quadrupolar parameters were taken from the fitted values as depicted in Figure S10, while for boron they were taken from DFT calculations: (C_Q, η_Q) = (0.1 MHz, 0.4). Previous comparison of the experimental and calculated ^{23}Na quadrupolar parameters showed the DFT calculations to be accurate. The dashed line indicates an Arrhenius fit to the data in the cubic (high-temperature) phase with activation energy E_a = 450 meV for sodium and 400 meV for boron.

Table of Contents
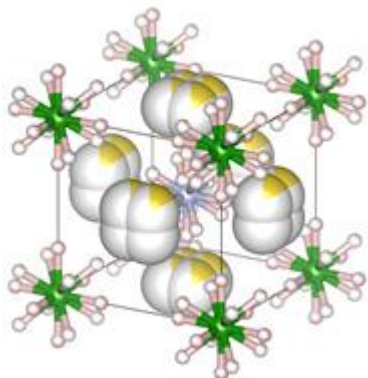
An antiperovskite sodium ion conductor is shown to benefit from a double paddle-wheel effect whereby the translation of the sodium cation is aided by the rotation of two distinct cluster anions.